Contents lists available at ScienceDirect

# International Journal of Heat and Mass Transfer

journal homepage: www.elsevier.com/locate/hmt



# Extraction of thermal conductivity using phonon Boltzmann Transport Equation based simulation of frequency domain thermo-reflectance experiments



Siddharth Sauray, Sandip Mazumder\*

Department of Mechanical and Aerospace Engineering, The Ohio State University, Suite E410, Scott Laboratory, 201 West 19th Avenue, Columbus, OH 43210, USA

#### ARTICLE INFO

Article history: Received 21 December 2022 Revised 10 January 2023 Accepted 13 January 2023

Keywords: Thermoreflectance FDTR Phonon BTE Boltzmann Thermal conductivity

#### ABSTRACT

The multidimensional phonon Boltzmann Transport Equation (BTE) was solved numerically in cylindrical coordinates and in time domain to simulate a Frequency Domain Thermo-Reflectance (FDTR) experimental setup. The phase lag between the pump and probe laser signals were computed for a pump laser modulation frequency ranging from 20 to 200 MHz. Results were obtained both with and without the inclusion of optical phonons, as well as with two different relaxation time-scale expressions (Holland versus Broido) for scattering, obtained from the literature for silicon. It was found that inclusion of optical phonons significantly improved the agreement between the measured and the computed phase lag. Subsequently, the thermal conductivity was extracted by fitting the Fourier heat conduction equation results-also solved numerically in time domain-to the measured and computed (using BTE) phase lag values. While both relaxation time-scales exhibited thermal conductivity suppression, a clear superiority of one time-scale expression over the other could not be established. With the Broido time-scale, the thermal conductivity extracted from BTE calculations overpredicted the value extracted from experiments regardless of whether optical phonons were included in the calculations. In contrast, with the Holland time-scale, the extracted thermal conductivity value overpredicted the value extracted from experiments when optical phonons were included, but underpredicted the value when optical phonons were excluded. © 2023 Elsevier Ltd. All rights reserved.

# 1. Introduction

A commonly used noncontact optical pump probe technique for the study of thermal transport at small time and length scales, based on thermo-reflectance, is the Frequency Domain Thermo-Reflectance (FDTR) technique. By "small," it is meant scales comparable to or smaller than the mean free paths of the energy-carrying phonons in a semiconductor material. In an FDTR experiment, the sample is covered by a thin metallic layer called the *transducer*. It is heated using a modulated continuous wave pump laser beam resulting in surface temperature (reflectivity) oscillations. These oscillations are then monitored using a probe laser. The lag in phase between the pump and probe laser signals is recorded, and a thermal transport model is needed to establish the causal connection between the two signals and extract the thermal conductivity of the substrate from the measured phase lag.

E-mail address: mazumder.2@osu.edu (S. Mazumder).

The solution of the Fourier heat conduction equation in frequency domain is the most common and earliest model used for this purpose. Brought to the limelight by Cahill [1], this approach has been used by many researchers since then [2,3]. Multiple layers, resulting from the use of a transducer, is treated using the Feldman algorithm [4]. Unfortunately, these closed-form analytical models are unable to distinguish between changes made to the pump laser spot size (diameter) versus the probe laser spot size [5], since only the effective radius appears in the solution. The problem may be overcome by resorting to numerical solution of the Fourier heat conduction equation [5].

The thermal conductivity extracted from FDTR experiments using the Fourier heat conduction equation has been found to change when the modulation frequency of the pump laser is changed [1–3,6]. The Fourier law assumes that all phonons travel with infinite velocity and engage in infinite many scattering events regardless of the distance traversed. The dependence of thermal conductivity on the modulation frequency is attributed to the fact that when the laser modulation frequency is high, the thermal penetration depth, which is inversely proportional to the square root of the modulation frequency, is small, and can often be smaller than the mean

<sup>\*</sup> Corresponding author.

#### **Nomenclature** Α area [m<sup>2</sup>] specific heat capacity per unit volume $[J m^{-3} K^{-1}]$ С D density of states per unit volume [m<sup>-3</sup>] f number density function equilibrium number density function $f_0$ spectral directionally integrated intensity $G_{\omega,p}$ $[Wm^{-2} rad^{-}1 s]$ contact conductance [W m<sup>-2</sup> K<sup>-1</sup>] Dirac constant = 1.0546 6 $\times$ 10<sup>-34</sup> [m<sup>2</sup>kg.s<sup>-1</sup>] $G_C$ ħ spectral directional phonon intensity $I_{\omega,p}$ $[Wm^{-2}sr^{-1}rad^{-}1s]$ equilibrium phonon intensity [Wm<sup>-2</sup>sr<sup>-1</sup>rad<sup>-</sup>1 s] $I_{0,\omega,p}$ Boltzmann constant = $1.381 \times 10^{-23} \text{ [m}^2\text{kg.s}^{-2}\text{K}^{-1}\text{]}$ $k_B$ thermal conductivity of transducer [W m<sup>-1</sup> K<sup>-1</sup>] $k_T$ â unit surface normal vector $N_{band}$ total number of spectral intervals (or bands) $N_{dir}$ number of solid angles (or directions) phonon polarization index р heat flux vector [Wm<sup>-2</sup>] q Q heat transfer rate [W] radial coordinate or radius [m] r r position vector [m] ŝ unit direction vector t time [s] Τ absolute temperature [K] internal energy $[J m^{-3}]$ и V volume of cell [m<sup>3</sup>] axial coordinate or thickness [m] z Greek density of transducer [kg m<sup>-3</sup>] $\rho_T$ polar angle [radians] $\theta$ phonon group velocity vector [m s<sup>-1</sup>] $\boldsymbol{v}_{\omega,\,p}$ spectral relaxation time scale [s] $\tau_{\omega,p}$ angular frequency [rad s<sup>-1</sup>] ω modulation frequency of pump laser [Hz] $\omega_L$ solid angle (sr) Ω azimuthal angle [rad]

free path of some of the energy-carrying phonons. As a result, some phonons hardly scatter. This results in so-called ballistic-diffusive transport or quasi-ballistic transport. In this regime of transport, the effective thermal conductivity has been found to be smaller than the bulk value—a phenomenon known as *thermal conductivity suppression* [6–8].

Various enhancements to Fourier law-based models have been proposed in an effort to capture the ballistic effects and predict the thermal conductivity suppression for different modulation frequencies. One class of these models [9] makes use of the hyperbolic heat conduction equation which accounts for finite velocity of the phonons by introducing a relaxation time as a parameter [10]. However, all phonons are assumed to have the same velocity irrespective of their type and frequency. Two parameter models [11] have been used to treat the diffuse and ballistic phonons differently by introducing an additional term in the Fourier heat conduction equation that involves the characteristic ballistic heat transport length as an additional parameter. Ramu and Bowers [12] proposed a two-band model in which a cut-off frequency was used to classify the phonons into ballistic and diffusive phonons. The ballistic phonons were then treated by adding a higher order correction term to the Fourier law that was derived from the phonon BTE. In a similar ballistic-diffusive model proposed by Chen [13], and later expanded to complex three-dimensional geometry by Mittal and Mazumder [14,15], the phonon intensity was split into a diffusive component and a ballistic component. More recently, a model that introduces a hydrodynamic term in the Fourier heat conduction equation—analogous to the advective term in the Navier-Stokes equation—has been proposed to capture ballistic effects [16]. Other studies have attempted to reconcile the poor agreement (lack of fit) of Fourier heat conduction equation-based predictions to measured phase lag by using anisotropic thermal conductivity (different thermal conductivity value in throughand in-plane directions) [17,18].

The development of the aforementioned approximate models has been partly prompted by the fact that the full-fledged phonon BTE is very challenging and time consuming to solve [19], although promising new algorithmic developments have been made on this front recently [20,21]. Peraud and Hadjiconstantinou [22] performed Monte Carlo simulations of phonon transport in a multidimensional optical pump-probe setup by using an energy-based deviational formulation. Only a single laser pulse was considered. This code was later used by Ding et al. [23] to simulate a single laser pulse of a TDTR experiment to demonstrate in-plane and through-plane thermal conductivity suppression. Regner et al. [24] solved the one-dimensional (1D) BTE in frequency domain to extract the thermal conductivity accumulation and suppression functions. However, the influence of multidimensional thermal transport can only be captured by solving the multidimensional BTE. Ali et al. [25] solved the full phonon BTE for TDTR experiments in a 2D planar setup and the model demonstrated thermal conductivity suppression and its dependence on the modulation frequency of the pump laser without the use of any additional tuning parameters. In a recent preliminary study, Saurav and Mazumder [26] demonstrated solution of the BTE in a 2D axisymmetric domain (as opposed to 2D planar [25]) for simulation of an FDTR experiment. The solution was advanced in time to a quasi-periodic state, enabling reliable extraction of the phase lag. This is in contrast with previous studies [22,23] that only simulated a single laser pulse. Although preliminary, this demonstration laid the foundation for the present study wherein the BTE solver was further enhanced to include optical phonons, and the thermal conductivity was subsequently extracted. To the best of the authors' knowledge, this study represents the first of its kind in which thermal conductivity has been extracted from multidimensional BTE simulation of an FDTR experimental setup.

# 2. Theory

# 2.1. The phonon Boltzmann Transport Equation (BTE)

The BTE is appropriate for modeling phonon transport in semiconductors, as phonons follow Bose-Einstein statistics and interact with each other via scattering events. The phonon BTE, under the single relaxation time approximation can be written as [9,19]

$$\frac{\partial f}{\partial t} + \boldsymbol{v} \cdot \nabla f = \frac{f_0 - f}{\tau},\tag{1}$$

where f is the distribution function of an ensemble of phonons,  $f_0$  is the equilibrium number density function, $\tau$  is the scattering time scale and vis the phonon group velocity. In general,  $f = f(t, \mathbf{r}, \mathbf{K})$ , where  $\mathbf{r}$  denotes the position vector and  $\mathbf{K}$  denotes the wavevector. Here, it is assumed that the wave-vector space is isotropic. Hence, it can be expressed conveniently [9] using a unit direction vector,  $\hat{\mathbf{s}}$ , and a frequency,  $\omega$ . Thus, the distribution function, f, for each polarization p, is a function of seven independent variables, i.e.,  $f = f(t, \mathbf{r}, \hat{\mathbf{s}}, \omega, p)$ , where the unit direction vector,  $\hat{\mathbf{s}}$ , may be expressed in terms of the azimuthal angle,  $\psi$ , and polar angle,  $\theta$ , as [27]

$$\hat{\mathbf{s}} = \sin\theta \cos\psi \,\hat{\mathbf{i}} + \sin\theta \sin\psi \,\hat{\mathbf{j}} + \cos\theta \,\hat{\mathbf{k}}. \tag{2}$$

If the Cartesian coordinate system is used to describe space, for example, one may write the functional dependence of f as  $f = f(t,x,y,z,\theta,\psi,\omega,p)$ . In other words, for a three-dimensional (3D) geometry, f is a function of 8 independent variables. Since polarizations are discrete, it is customary to think of f as being a function of 7 independent variables, with the implicit understanding that it is different for different polarizations. The group velocity is also dependent on direction:  $\mathbf{v} = \mathbf{v}(\hat{\mathbf{s}},\omega,p)$ . The equilibrium Bose-Einstein distribution, on the other hand, is direction independent:  $f_0 = f_0(\omega,T)$ , as is the relaxation time-scale:  $\tau = \tau(\omega,T,p)$ . Following the seminal work of Majumdar [28], a phonon intensity may be defined in terms of the distribution function:

$$I_{\omega,p} = I(t, \mathbf{r}, \hat{\mathbf{s}}, \omega, p) = |\mathbf{v}_{\omega,p}| \hbar \omega f D(\omega, p) / 4\pi$$
  

$$I_{0,\omega,p} = I_0(t, \mathbf{r}, \omega, p) = |\mathbf{v}_{\omega,p}| \hbar \omega f_0 D(\omega, p) / 4\pi$$
(3)

where  $D(\omega, p)$  is the density of states, and  $I_{\omega,p}$  is the spectral directional phonon intensity, while  $I_{0,\omega,p}$  is the equilibrium spectral phonon intensity. Substitution of Eq. (3) into Eq. (1) yields [28]

$$\frac{\partial I_{\omega,p}}{\partial t} + \boldsymbol{v}_{\omega,p} \cdot \nabla I_{\omega,p} = \frac{I_{0,\omega,p} - I_{\omega,p}}{\tau_{\omega,p}}.$$
 (4)

For any given frequency and polarization, the intensity,  $I_{\omega,p}$ , is a function of time, 3 space variables (in 3D), and 2 directional variables, making Eq. (4) a six-dimensional equation. Furthermore, it needs to be solved for all frequency and polarizations in order to determine the heat flux, as is discussed in the sub-section to follow.

Solution of the BTE [Eq. (4)] necessitates boundary conditions for the intensity. Two types of boundary conditions are generally used: (1) thermalizing, and (2) reflective. At a thermalizing boundary, phonons are emitted from it based on the equilibrium energy distribution and any phonon that strikes it immediately gets absorbed. The boundary condition is mathematically written as  $I_{\omega,p}(t,\mathbf{r}_w,\mathbf{\hat{s}}_o,\omega,p)=I_{0,\omega,p}(t,\mathbf{r}_w,\omega,p)$ , where  $\mathbf{r}_w$  is the position vector of the boundary or wall, and  $\mathbf{\hat{s}}_o$  is the outgoing direction for the intensity.

# 2.2. Heat flux and energy conservation (first law)

Once the BTE [Eq. (4)] has been solved, the heat flux may be calculated from the phonon intensity using the relationship [19]

$$\mathbf{q}(t,\mathbf{r}) = \sum_{p} \int_{\omega_{\min,p}}^{\omega_{\max,p}} \int_{4\pi} I_{\omega,p}(t,\mathbf{r},\hat{\mathbf{s}},\omega,p) \hat{\mathbf{s}} d\Omega d\omega = \sum_{p} \int_{\omega_{\min,p}}^{\omega_{\max,p}} \mathbf{q}_{\omega,p}(t,\mathbf{r}) d\omega$$
(5)

where the integrals are over all solid angles  $\Omega$  and the frequency range of each polarization;  $\omega_{\max,p}$  and  $\omega_{\min,p}$  are the maximum and minimum frequencies, respectively, corresponding to a given polarization, p. In Eq. (5),  $\mathbf{q}_{\omega,p}$  denotes the spectral heat flux while  $\mathbf{q}$  denotes the total heat flux. Substitution of Eqs. (4) and (5) into the energy conservation equation (First Law), followed by some manipulation, yields [19]:

$$\begin{split} &\frac{\partial}{\partial t} \left( \sum_{p} \int\limits_{\omega_{\min,p}}^{\omega_{\max,p}} \frac{\hbar \omega D(\omega,p)}{\exp[\hbar \omega/k_{B}T]-1} d\omega \right) = \\ &- \sum_{p} \int\limits_{\omega_{\min,p}}^{\omega_{\max,p}} \frac{1}{|u_{\omega,p}|} \left[ \frac{1}{\tau_{\omega,p}} \left( \frac{|u_{\omega,p}| \hbar \omega D(\omega,p)}{\exp[\hbar \omega/k_{B}T]-1} - G_{\omega,p} \right) - \frac{\partial G_{\omega,p}}{\partial t} \right] d\omega \end{split} \tag{6}$$

where

$$G_{\omega,p} = \int_{4\pi} I_{\omega,p} d\Omega. \tag{7}$$

Eq. (6) is a nonlinear equation that may be solved to obtain the so-called pseudo-temperature [19,29], *T*, at any location within the computational domain and any instant of time. In the section to follow, numerical techniques for solution of the BTE are discussed.

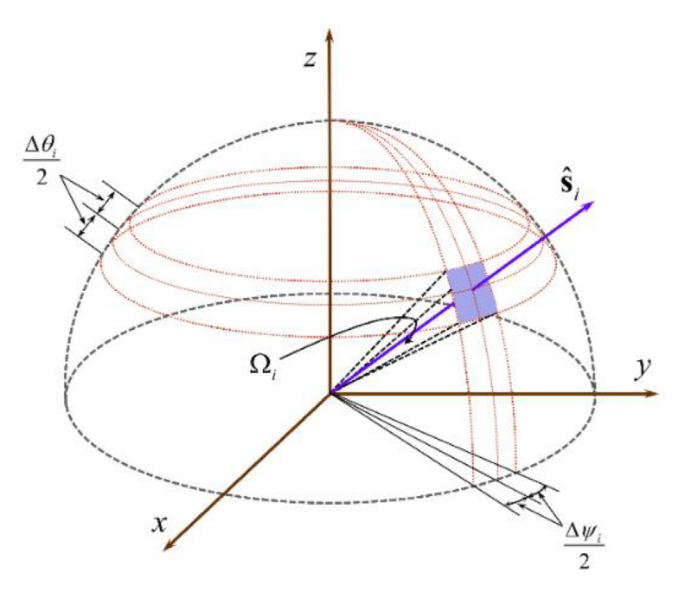


Fig. 1. Polar coordinate system used for angular discretization in the FAM.

# 3. Numerical procedure

The present work uses the finite angle method (FAM) [19,27] for solving the BTE [Eq. (4)]. It is briefly discussed next, along with treatment of the transducer, which is a metallic film that covers the substrate.

#### 3.1. The finite angle method (FAM)

The FAM is a variant of the Discrete Ordinates Method [27]. In the FAM, the entire solid angle space is first split into a set of nonoverlapping smaller solid angles. These smaller solid angles may be based on equal subdivisions in  $\theta$  and  $\psi$ , as shown in Fig. 1. The BTE [Eq. (4)] is first integrated over a volume [finite volume method in space on a structured mesh with cell index (j,k)], followed by finite solid angles to yield [19,27]:

$$\frac{\partial I_{i,\omega,p}}{\partial t} \bigg|_{(j,k)} V_{(j,k)} \Omega_i + |\boldsymbol{v}_{\omega,p}| \sum_{f=1}^{N_{f,k}} I_{i,\omega,p,f(j,k)} (\mathbf{S}_i \cdot \hat{\mathbf{n}}_f) A_{f(j,k)}$$

$$= \frac{1}{\tau_{\omega,p,(j,k)}} (I_{o,\omega,p,(j,k)} - I_{i,\omega,p,(j,k)}) V_{(j,k)} \Omega_i \, \forall \, i = 1, 2, ..., N_{dir} \quad (8)$$

where  $N_{dir}$  is the total number of discrete directions or finite solid angles,  $V_{(j,k)}$  is the volume of the (j,k)-th cell,  $A_{f(j,k)}$  is the area of the f-th face of the (j,k)-th cell, and

$$\Omega_{i} = \int_{\Delta\Omega_{i}} \Omega = \int_{\theta_{i} - \Delta\theta_{i}/2\psi_{i} - \Delta\psi_{i}/2}^{\theta_{i} + \Delta\theta_{i}/2\psi_{i} + \Delta\psi_{i}/2} \sin\theta \, d\theta \, d\psi$$

$$= 2\sin\theta_{i}\sin\left(\frac{\Delta\psi_{i}}{2}\right)\Delta\psi_{i} \tag{9}$$

anc

$$\mathbf{S}_{i} = \cos \psi_{i} \sin \left(\frac{\Delta \psi_{i}}{2}\right) [\Delta \theta_{i} - \cos(2\theta_{i}) \sin(\Delta \theta_{i})] \hat{\mathbf{i}}$$

$$+ \sin \psi_{i} \sin \left(\frac{\Delta \psi_{i}}{2}\right) [\Delta \theta_{i} - \cos(2\theta_{i}) \sin(\Delta \theta_{i})] \hat{\mathbf{j}}$$

$$+ \left(\frac{\Delta \psi_{i}}{2}\right) \sin(2\theta_{i}) \sin(\Delta \theta_{i}) \hat{\mathbf{k}}$$
(10)

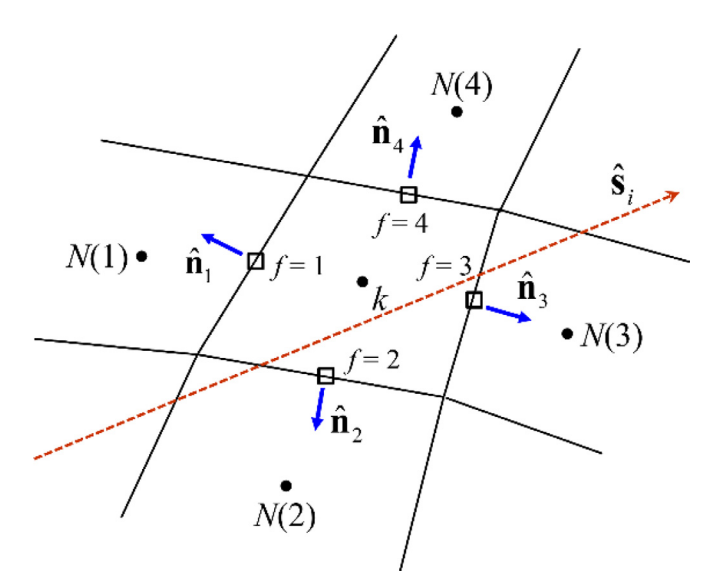


Fig. 2. Schematic representation of geometric quantities used for finite volume discretization of the BTE.

The subscript i for the intensity now denotes an intensity along a line of sight passing through the center of the solid angle, i.e., in the direction  $\hat{\mathbf{s}}_i$  (see Fig. 1). Finally, the face intensity in Eq. (8) is expressed in terms of cell-center intensities using the first-order upwind or step scheme [27]:

$$I_{i,\omega,p,f(j,k)} = \begin{cases} I_{i,\omega,p,j,k} \text{if } \hat{\mathbf{s}}_i \cdot \hat{\mathbf{n}}_f > 0 \\ I_{i,\omega,p,N(f)} \text{if } \hat{\mathbf{s}}_i \cdot \hat{\mathbf{n}}_f < 0 \end{cases}$$
(11)

where N(f) denotes the neighboring cell next to face f, as shown in Fig. 2.

As a final note, in cylindrical coordinates, the volume appearing in Eq. (8) may be determined using  $V_{(j,k)} = \int\limits_{z_{b(j,k)}}^{z_{t(j,k)}} \int\limits_{r_{i(j,k)}}^{r_{o(j,k)}} 2\pi r dr dz$ ,

where  $r_{i(j,k)}$  and  $r_{o(j,k)}$  are inner and outer radii, respectively, of the (j,k)-th cell, while  $z_{b(j,k)}$  and  $z_{t(j,k)}$  are bottom and top z-coordinates, respectively, of the same cell, as shown on Figs. 3 and 4. For any horizontal face, the area is given by  $A_{f(j,k)} = \pi \, (r_{o(j,k)}^2 - r_{i(j,k)}^2)$ , while for any vertical face, the area is given by  $A_{f(j,k)} = 2\pi r_f(z_{t(j,k)} - z_{b(j,k)})$ .

# 3.2. Treatment of the transducer

The transducer is metallic. In this study, heat conduction in the transducer is treated using the Fourier law. Furthermore, since the transducer is very thin, it is assumed that there is no temperature variation within the transducer in the z direction (Fig. 3). The only variation is in the r direction. With this premise, the computational domain may be discretized using a structured mesh in the r-z plane, as shown in Fig. 4.

The governing equation for heat transfer in the transducer may be derived from an energy balance, and is written as

$$\rho_{T}c_{T}\frac{\partial T_{T}}{\partial t} = \frac{k_{T}}{r}\frac{\partial}{\partial r}\left(r\frac{\partial T_{T}}{\partial r}\right) + \frac{(q_{t}^{''} - q_{b}^{''})}{z_{T}}$$
(12)

where  $\rho_T$ ,  $c_T$ ,  $k_T$ , and  $z_T$  are the density, specific heat capacity, thermal conductivity, and thickness of the transducer, respectively. The temperature of the transducer is denoted by  $T_T$ . The heat fluxes at the top and bottom surfaces of the transducer are denoted by  $q''_t$  and  $q''_b$ , respectively. The heat flux on the top surface is the energy supplied by the pump laser, and is a known quantity, written as

$$q''_{t} = q''_{l}(r)[1 + \sin \omega_{l}t] \tag{13}$$

where  $q^{''}_{L}(r)$  is the radially varying (such as Gaussian) laser flux, and  $\omega_{L}$  is the modulation frequency of the pump laser. The heat flux on the bottom surface of the transducer is not a known quantity. However, it can be related to the substrate through the relationship

$$q''_{b} = G_{C}(T_{T} - T_{top}) (14)$$

where  $T_{top}$  is the temperature on the top of the substrate surface, and  $G_C$  is the contact conductance between the transducer and the substrate. Although  $T_{top}$  is not directly known, it can be derived from the solution (of temperature) in the substrate, which in turn, requires solution of the BTE. Thus, coupling the transducer to the substrate requires a self-consistent procedure. This procedure is described in the section to follow.

As a final step, applying the finite-volume procedure [30] for discretization of Eq. (12), along with explicit (forward Euler) time discretization, we obtain

$$\rho_{T} c_{T} z_{T} \frac{2r_{j} \Delta r_{j}}{\Delta t} \left[ T_{T,j} - T_{T,j}^{old} \right] = 2q''_{t,j} r_{j} \Delta r_{j} - 2q''_{b,j} r_{j} \Delta r_{j} 
- \left[ \frac{k_{T} z_{T} (2r_{j} + \Delta r_{j})}{\Delta r_{j} + \Delta r_{j+1}} \right] T_{T,j+1}^{old} - \left[ \frac{k_{T} z_{T} (2r_{j} - \Delta r_{j})}{\Delta r_{j} + \Delta r_{j-1}} \right] T_{T,j-1}^{old} 
- \left[ \frac{k_{T} z_{T} (2r_{j} + \Delta r_{j})}{\Delta r_{j} + \Delta r_{j+1}} + \frac{k_{T} z_{T} (2r_{j} - \Delta r_{j})}{\Delta r_{j} + \Delta r_{j-1}} \right] T_{T,j}^{old}$$
(15)

where the superscript "old" represents values at the previous timestep.

# 3.3. Solution algorithm

Determination of the (pseudo-)temperature and heat flux in an FDTR setup using the explicit (or forward Euler) time marching procedure requires the following steps:

- 1. The temperature of the entire solution (computational) domain is first initialized. This includes nonisothermal boundaries, such as the transducer top.
- 2. The BTE [Eq. (4)] is marched forward explicitly by one time step to determine the spectral intensity,  $I_{\omega,p}$ . This intensity is then post-processed to compute the incident phonon intensity,  $G_{\omega,p}$ , using Eq. (7). Likewise, Eq. (5) may be used to compute the heat flux at locations of interest, e.g., at boundary surfaces.
- 3. The computed value of  $G_{\omega,p}$  is then substituted into Eq. (6) and the resulting equation is solved using a nonlinear equation solver to determine the pseudo-temperature at any given location in space and instant of time.
- 4. The intensities obtained from the solution of the BTE can also be used to determine the heat flux at the top surface of the substrate using Eq. (5).
- 5. The heat flux at the top surface of the substrate is equal to the heat flux at the bottom surface of the transducer,  $q''_{b,j}$ . Once this is known, Eq. (15) can be marched forward in time. Solution of Eq. (15) yields the transducer temperature.
- 6. With the heat flux and transducer temperature both being known, the temperature on the top of the substrate can now be computed using Eq. (14). This new temperature replaces the initial condition in Step 1.
- 7. Steps 2–6 are repeated, i.e., the solution is marched forward in time.

# 4. Results and discussion

For the purposes of this study, the experimental data reported by Regner et al. [2] was used for comparison. The substrate in this experiment is a silicon block that is 525  $\mu$ m thick, and the radial (lateral) extent of substrate is not known. Several preliminary calculations were first conducted to estimate the thermal penetration

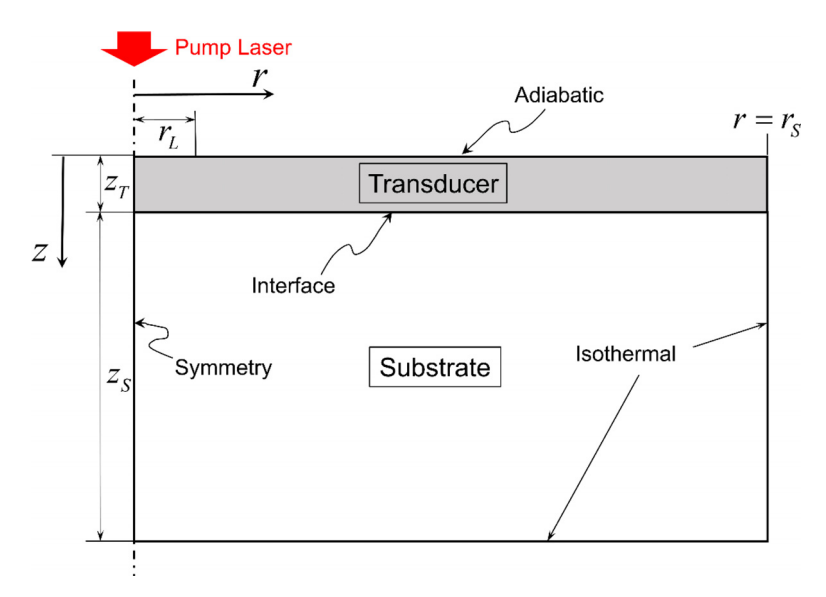


Fig. 3. Two-dimensional axisymmetric representation of an FDTR experimental setup.

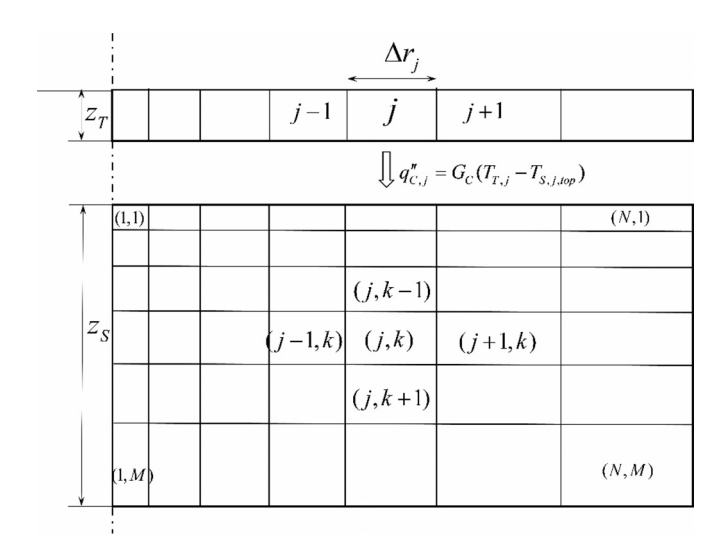


Fig. 4. Structured mesh in the r-z plane used to discretize the substrate and the transducer.

depth (which indirectly affects the computational domain size) for the full range of modulation frequencies, and the grid density necessary to adequately resolve the heat wave. Following this study, a computational domain with  $z_s$ = 100  $\mu$ m and  $r_s$ = 100  $\mu$ m was deemed adequate. Isothermal boundary conditions (300 K) were applied to the side and bottom surfaces of the substrate, while an adiabatic boundary condition was applied to the top surface of the transducer beyond the laser spot. In a previous study [5], Newton cooling boundary conditions, with heat transfer coefficients consistent with natural convection, were used for all of these boundary conditions, and it was found that the results did not change compared to the boundary conditions used here. The transducer is a bilayer transducer with 55 nm of gold and 5 nm of chromium, resulting in  $z_T = 60$  nm. The thermophysical properties of gold and chromium that were used for calculations are shown in Table 1. Based on the thicknesses of the gold and chromium layers, effective values of the properties of the transducer were estimated and used. These are also shown in Table 1.

For numerical calculations, a  $120 \times 120$  nonuniform mesh with a stretching factor not exceeding 1.05 was used, as shown schematically in Fig. 4. The minimum grid size used in either direction is

**Table 1**Thermophysical properties of the various materials used in the calculations.

	Silicon (bulk)	Transducer		
		Gold	Chromium	Effective
Density (kg/m³) Specific heat capacity (J/kg/K) Thermal conductivity (W/m/K)	2329 702 148	19,320 129 310	7140 450 93.9	18,290.8 155.7 266.6

30 nm. The modulation frequency, which is an input parameter, was varied between 20 MHz and 200 MHz, with 8 different frequencies. Each sinusoidal cycle of the laser was split into 5000 time-steps, which was deemed appropriate after a time-step independence study. This implies that a time-step size of 1 ps was used. This time-step size also obeys the stability criterion of the explicit method being used here. Furthermore, it is small enough to resolve the scattering events. The nominal value of the interfacial (between the substrate and the transducer) contact conductance,  $G_C$ , was taken to be 200 MW/m<sup>2</sup>/K, as suggested by Cahill [1], although for a different material pair. The pump and probe laser  $1/e^2$  radii are inputs in the model. Here,  $r_{pump}=4.1\mu \text{m}$ and  $r_{probe} = 2.8 \mu \text{m}$  were used. A Gaussian laser flux profile (in r) was used for all calculations. The frequency space was discretized, as shown in Fig. 5, with  $N_{TA} = 14$ ,  $N_{LA} = 24$ , and  $N_{TO} = N_{LO} = 1$ . The decision to use 1 band for each optical phonon branch was prompted by the fact that the frequency range of the optical phonons in silicon is only about 20% that of the total range (Fig. 5). Furthermore, previous studies [31,32] suggest that 1 band is sufficient to resolve each optical phonon type. The spectral discretization of the frequency space for acoustic phonons is also based on previous studies [25,33] and a recent study [34] that concludes that ~60 bands are needed to capture dispersion in most materials, including compound semiconductors. The angular space was discretized using 4 azimuthal angles and 20 polar angles, resulting in a total of 80 finite solid angles or directions.

Scattering of phonons has been treated using a variety of approaches ranging all the way from scattering time-scales derived from ab initio calculations with full treatment of the anisotropic Brillouin zone [35–37] to simplified parameterized single-time relaxation time-scale expressions. Here, the latter approach is used in keeping with the assumption of an isotropic wave-vector space (see Section 2.1) and also because these parameterized scattering time-scale expressions have been routinely used in engineering

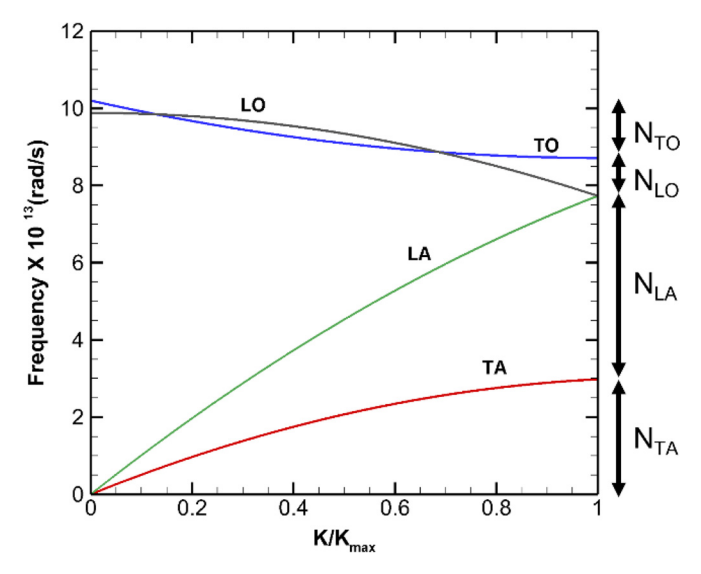


**Fig. 5.** Dispersion relation of silicon from [29]; discretization of the frequency space is also shown.

calculations [25,29,32,33,38,39]. For the scattering (or relaxation) time-scales of acoustic phonons, two different models were used in this study:

Broido and co-workers [40]:

$$\tau_{N,p}^{-1} = A_p^N \omega^2 T [1 - \exp(-3T/\theta_D)]$$
 (16a)

$$\tau_{U,p}^{-1} = A_p^U \omega^4 T [1 - \exp(-3T/\theta_D)]$$
 (16b)

where the subscripts N and U stand for Normal and Umklapp processes, respectively, and the subscript p stands for the polarization of the phonon, i.e., either longitudinal acoustic (LA) or transverse acoustic (TA). The constants in Eq. (16) are as follows: $A_{LA}^N = 7.10 \times 10^{-20} \text{s.rad}^{-2} \text{K}^{-1}$ ,  $A_{TA}^N = 10.9 \times 10^{-20} \text{s.rad}^{-2} \text{K}^{-1}$ ,  $A_{LA}^U = 9.51 \times 10^{-47} \text{s}^3$ .rad<sup>-4</sup>K<sup>-1</sup>, and  $A_{TA}^U = 37.8 \times 10^{-47} \text{s}^3$ .rad<sup>-4</sup>K<sup>-1</sup>. It is worth noting that although this model is parameterized (primarily, to allow convenient use), it was derived from first principles [40].

Holland [41]:

$$\tau^{-1} = B_I \omega^2 T^3 (Normal and Umklapp, LA), \tag{17a}$$

$$\tau^{-1} = B_{TN}\omega T^4(Normal, TA), \tag{17b}$$

$$\tau^{-1} = \begin{cases} 0 & \text{if} \quad \omega < \omega_{1/2} \\ B_{TU}\omega^2 \sinh(\hbar\omega/k_BT) & \text{if} \quad \omega \ge \omega_{1/2} \end{cases} \quad (Umklapp, TA),$$
(17c)

where the constants in Eq. (17) are as follows:  $\omega_{1/2}=2.418\times 10^{13}$  rad/s,  $B_L=2\times 10^{-24}~{\rm K}^{-3}{\rm rad}^{-2}~{\rm s}$ ,  $B_{TN}=9.3\times 10^{-13}{\rm K}^{-4}{\rm rad}^{-1}$ , and  $B_{TU}=5.5\times 10^{-18}{\rm rad}^{-2}~{\rm s}$ .

Optical phonons were also considered in this study. Although it is generally believed that optical phonons do not contribute significantly to thermal transport in silicon except at high temperature [32] because of their low group velocities, they do contribute significantly to storage of energy. Hence, they have the ability to affect the thermal diffusivity and, thereby, the phase lag. To highlight this point, for a crystalline material, the internal energy and the specific heat capacity at constant volume, which is the derivative of internal energy with respect to temperature, are given by [19]

$$u = \sum_{p} \int_{\omega_{\min p}}^{\omega_{\max,p}} \frac{\hbar \omega D(\omega, p)}{\exp[\hbar \omega / k_B T] - 1} d\omega$$
 (18a)

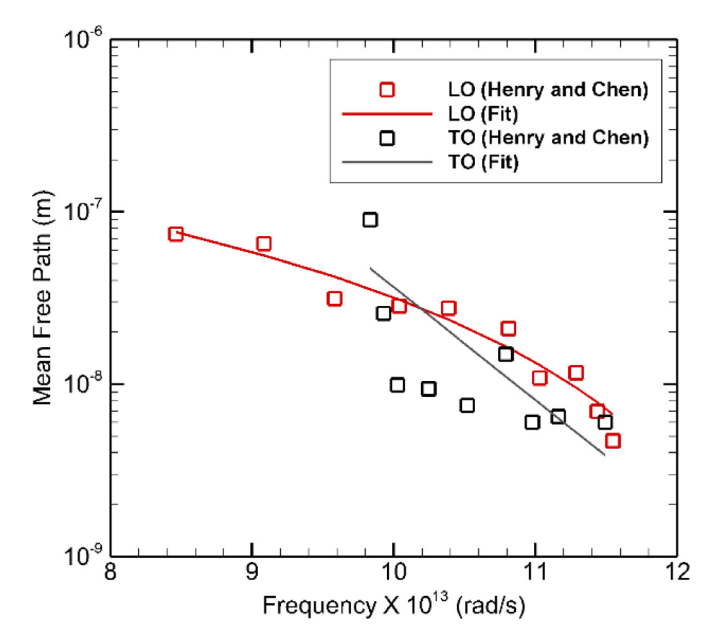


**Fig. 6.** Spectral mean free path of optical phonons, obtained from Henry and Chen [33], along with least-square curve-fits for the same data. LO = Longitudinal Optical; TO = Transverse Optical.

$$c = \frac{du}{dT} = \frac{\hbar^2}{k_B T^2} \sum_{p} \int_{\omega_{\text{min, p}}}^{\omega_{\text{max, p}}} \frac{\omega^2 D(\omega, p) \exp[\hbar \omega / k_B T]}{\left(\exp[\hbar \omega / k_B T] - 1\right)^2} d\omega$$
 (18b)

Eq. (18b), when used in conjunction with the dispersion relations shown in Fig. 5 to compute the specific heat capacity of silicon at 300 K, yields values of 325.4 J/kg/K and 625.4 J/kg/K without and with optical phonons, respectively. In other words, the ability to store heat by the material increases almost by a factor of two when optical phonons are included. This is consistent with the notion that optical phonons often serve as "reservoirs" of energy [9,31]. The final point to note in this regard is that the computed value of the specific heat capacity with optical phonons, namely 625.4 J/kg/K is much closer to the reported bulk value of 702 J/kg/K at 300 K.

Limited data is available on the relaxation time-scale for optical phonon scattering in silicon. In this study, the data published by Henry and Chen [42] were used. Fig. 6 shows the spectral mean free path data along with least-square curve-fits that were used to represent that scattered data in the present computations. The curve-fit expressions are as follows:

$$\Lambda_{LO} = A_{LO}\omega^2 + B_{LO}\omega + C_{LO} \tag{19a}$$

$$\Lambda_{TO} = A_{TO} \exp(-B_{TO}\omega) \tag{19b}$$

where  $\Lambda$  is the mean free path in meters, while  $\omega$  is the frequency in rad/s. The constants in Eq. (19) are as follows:  $A_{LO}=4.065\times 10^{-35}$ ,  $B_{LO}=-1.039\times 10^{-20}$ ,  $C_{LO}=6.641\times 10^{-7}$ ,  $A_{TO}=0.1254$ , and  $B_{TO}=1.51\times 10^{-13}$ . The relaxation time-scale for optical phonon scattering was computed using  $\tau=\Lambda/\upsilon$ . The dispersion relationships for silicon, shown in Fig. 5, adopted from Pop [31], were used to compute the phonon group velocities,  $\upsilon$ , for all frequencies and polarizations. As stated earlier, it is assumed that the wave-vector space is isotropic and, therefore, the dispersion relationship in only one lattice direction is necessary. Once the relaxation time-scales of the various phonons were computed, the Mathiessen rule [9] was used to compute the overall relaxation time-scale for scattering.

To bring to light the difficulty of BTE calculations for the problem at hand, a rough estimate is helpful. Since 40 bands

and 80 angles are used, the calculation essentially boils down to time-marching 3200 partial differential equations on a mesh with 14,400 cells. For the 200 MHz modulation frequency, the time period for each cycle is 5 ns. Since a time-step size of 1 ps is used, this means that the solution has to be advanced through roughly 25,000 time steps (5 cycles with 5000 time steps per cycle; see next paragraph for reasoning) before quasi-periodic state is reached. Using band-based parallelization over 40 processors (same as the number of bands), the calculations require approximately 7.5 h. However, for the 20 MHz modulation frequency, since the stability criterion of the explicit method dictates that the same time step size of 1 ps is to be used (Note: stability criterion depends on phonon speed and grid size, both of which are independent of modulation frequency), the calculation requires approximately 75 h. To keep computational times tractable, and also noting that the quasi-ballistic nature of phonon transport is primarily manifested at higher modulation frequencies, calculations for lower frequencies were not undertaken. An implicit time-marching scheme was also explored but was found to be computationally more expensive. Furthermore, it was found that using larger timestep size (which is allowable in implicit time-marching methods and is considered an advantage of such a method) negatively affected the accuracy of the computed phase.

For each simulation, the solution was advanced far enough in time such that the solution became quasi-periodic. The temperature of the transducer, averaged over the probe radius (or spot), was compared against the sinusoidal pump laser flux pulse, and the phase lag was computed. This was done in two ways: (1) using the time lag from peak to peak, and (2) using the time lag from trough to trough. Fig. 7 shows how the phase lag computed with these two approaches converge to a unique value as quasi-periodic state is approached. It also clearly demonstrates that the phase lag

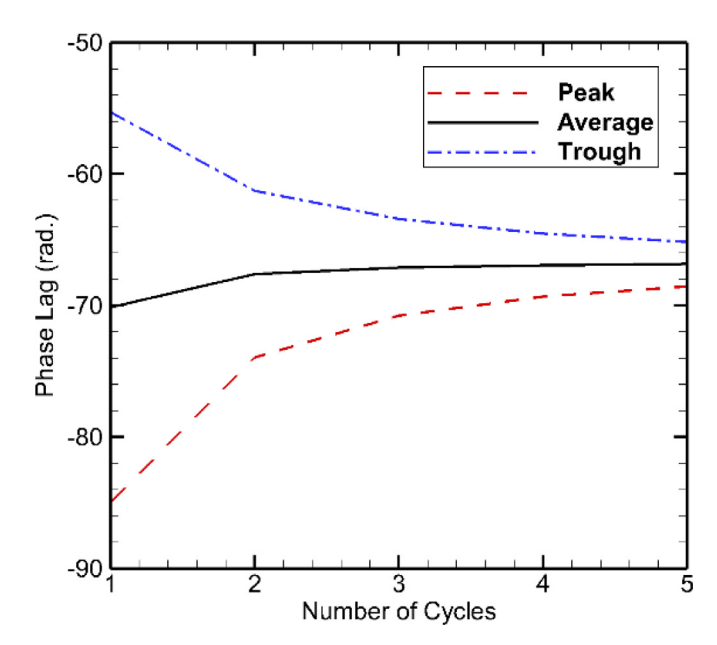


**Fig. 7.** Convergence of phase lag using two different approaches as the solution approaches quasi-periodic state.

converges to a unique value after about 5 pump laser cycles. A few cases were run for additional cycles but did not affect the computed phase lag.

Fig. 8 shows the temporal evolution of the nondimensional temperature  $[=(T-300)/(T_{\text{max}}-300)]$  distribution for a modulation frequency of 20 MHz with the two different relaxation time-

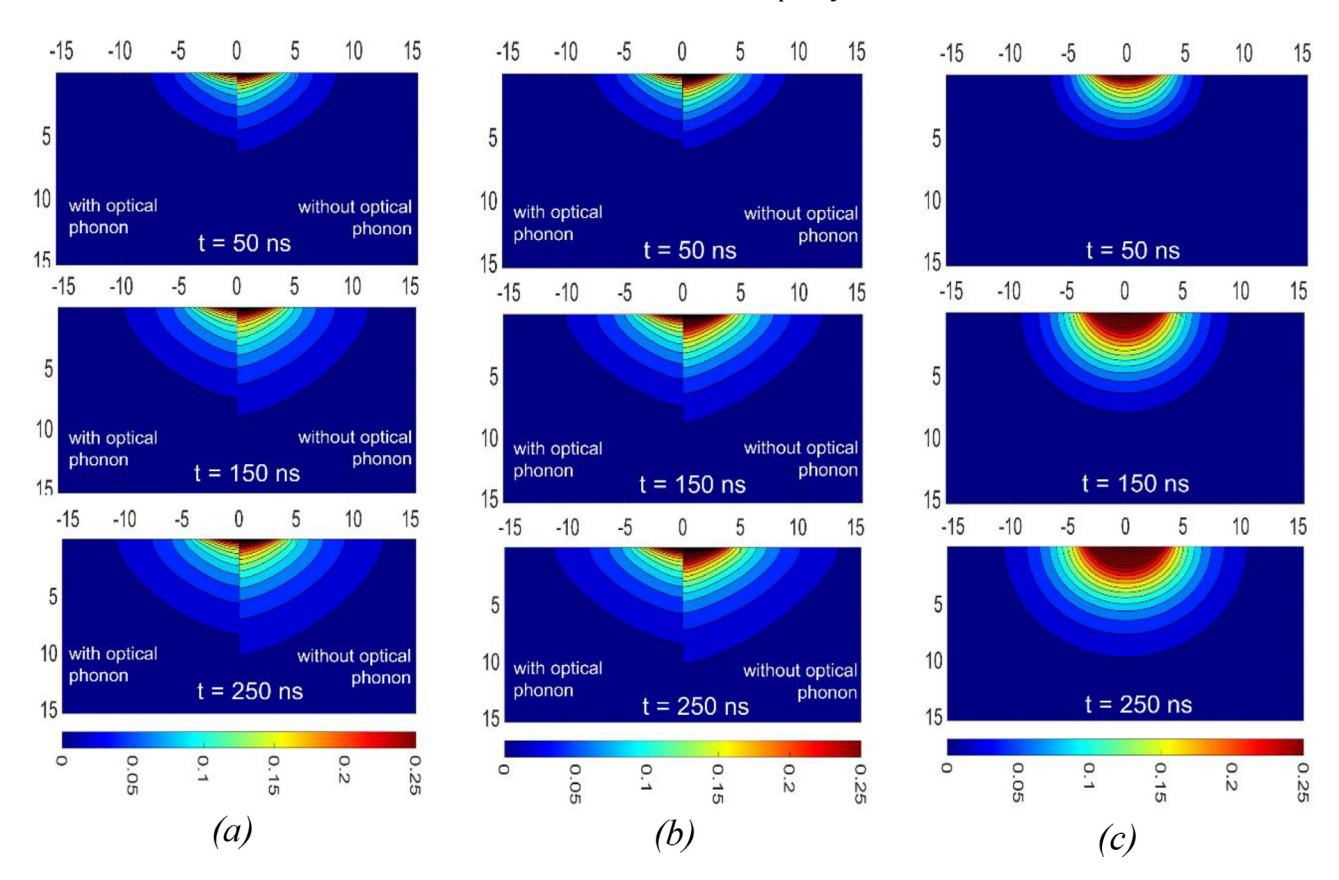


**Fig. 8.** Temporal evolution of the nondimensional temperature distribution for a modulation frequency of 20 MHz: (a) using the BTE with Broido time-scales, (b) using the BTE with Holland time-scales, and (c) using the Fourier heat conduction equation with k = 148 W/m/K. For clarity of figures, only a portion of the computational domain is shown. All dimensions are in  $\mu$ m.

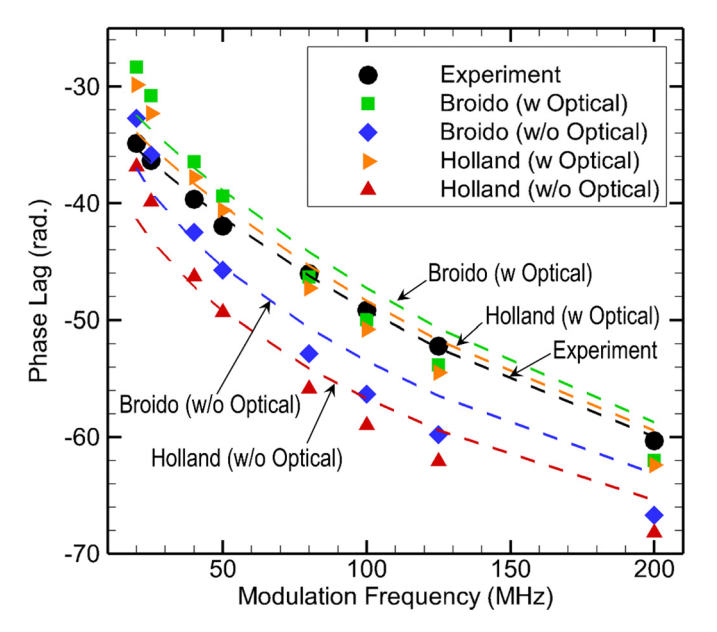


**Fig. 9.** Comparison of phase lag computed using the phonon BTE and experimentally measured values [2], both shown with symbols. The lines represent best fits to the data (symbols) using the Fourier heat conduction equation.

scale models for acoustic phonons and, also, with and without optical phonons. It appears that inclusion of optical phonons slows down the thermal front. As discussed earlier, optical phonons primarily contribute to storage of energy rather than enhancing transport. This results in reduced thermal diffusivity and slower spread of the thermal front. Comparison of Fig. 8(a) and (b) reveals that the use of the two different relaxation time-scale models for the acoustic phonons do not appear to significantly affect the results, at least qualitatively. Fig. 8(c), which was generated using the Fourier heat conduction equation with a thermal conductivity of 148 W/m/K, i.e., the bulk thermal conductivity of silicon at 300 K, shows a heat wave that is far more isotropic (semicircular) compared to the ones predicted by the BTE. Perhaps, this is an indication that the actual transport process, which is presumably better modeled by the BTE, is somewhat anisotropic. This finding appears to lend credibility to past hypotheses [17,18] of anisotropic transport, although this is not the focus of the present study and further investigations are warranted to confirm this hypothesis.

Fig. 9 shows the phase lag computed from the BTE results using both time-scale models as well as with and without optical phonons. Experimentally measured values are shown on the same plot for comparison. When optical phonons are included, both the Broido and the Holland time-scales appear to match experimentally measured values better, although at low frequencies the phase lag is underpredicted while at high frequencies, the phase lag is overpredicted by both models. Also, when optical phonons are included, the difference between the two models appear to become smaller. The role of optical phonons on thermal transport in silicon at steady state has already been studied [32]. It was found that they contribute about 5-10% to thermal transport at room temperature at steady state. However, it is worth noting that FDTR experiments are transient. Hence, how optical phonons alter thermal storage becomes equally important. As pointed out earlier in this section, optical phonons significantly alter the specific heat capacity. Consequently, they significantly alter the phase lag. Overall, the discrepancy between computed and measured phase lag may be attributed to several assumptions in the current model. First, it is the assumed that the interface conductance between the transducer and the silicon sample is fixed and a value of 200 MW/m<sup>2</sup>/K

**Table 2**Thermal conductivity of silicon (in W/m/K) extracted from BTE calculations and experimental data.

	Without optical phonons	With optical phonons
Experiment [2]	83	
BTE with Broido time-scale [30]	98	124
BTE with Holland time-scale [31]	65	106

was used. As stated earlier, this value is for a different material pair [1] and was used here for lack of better information. Secondly, it is assumed that the wave-vector space is isotropic and three-phonon scattering is adequately represented by the parameterized single-time relaxation time-scale expressions employed in this study.

As a final step, the Fourier heat equation was solved numerically in time domain following the procedure in [5] using the exact same settings (grid, time step, boundary conditions etc.) as that for the BTE code. The thermal conductivity, which appears as an input to the Fourier heat equation was adjusted until the best fit (based on minimization of the least-square error) was obtained to each of the datasets shown in Fig. 9. These best fits are depicted by dotted lines in Fig. 9. For these calculations, the bulk specific heat capacity value of 702 J/kg/K was used. It is important to note that the thermal conductivity is a parameter that appears only in the Fourier heat conduction equation and not in the BTE. Thus, it is not possible to extract the thermal conductivity directly from BTE calculations. Only an indirect method, in which the solution of the Fourier heat conduction equation is fitted to the solution of the BTE, can be used to extract the thermal conductivity from BTE results. Nonetheless, since the thermal conductivity is a quantity of engineering interest, such a practice is considered worthwhile, albeit somewhat questionable. Table 2 reports the thermal conductivity values that were extracted after fitting the datasets shown in Fig. 9. All values reported in the table exhibit thermal conductivity suppression, i.e., a reduction in its value from the bulk value of 148 W/m/K. The Broido time-scales yield less suppression compared to the Holland time-scales.

# 5. Summary and conclusions

It is now widely accepted that the BTE for phonons best encapsulates the physics of thermal transport in semiconductor materials at submicron scales. In this study, BTE computations are conducted in a two-dimensional axisymmetric geometry in cylindrical coordinates to simulate an FDTR experimental setup. The thin metallic transducer film is modeled using the Fourier law and radial conduction in the transducer is included. The governing equation in the transducer is coupled to the BTE calculations in the silicon substrate underneath. The BTE computations are performed with a computational mesh comprised of 14,400 quadrilateral control volumes. For angular discretization, 80 solid angles (directions) are used, while for discretization of the frequency space, 40 spectral intervals (or bands) are used. For time advancement, the explicit (forward Euler) procedure with equal time step size of 1 ps is used. Each simulation is carried out until quasi-periodic state is reached. This requires approximately 5 modulation cycles of the pump laser. The convergence of the phase lag was monitored to ascertain that the solution has been advanced sufficiently in time. Computations were performed for 8 different modulation frequencies ranging between 20 MHz and 200 MHz. The longest computations required approximately 75 h of wall clock time on a parallel computer system with 40 processors.

The scattering time-scales published by Ward and Briodo [40], as well as those by Holland [41], were used to model acoustic phonon scattering in this study. Furthermore, optical phonons were also included to isolate their effect on the extracted thermal conductivity. The time-scales for scattering of optical phonons was estimated from Henry and Chen [42]. With these time-scales as inputs, the BTE was solved and the phase lag between the pump and probe signals was computed. Results show that the extracted thermal conductivity increases significantly when optical phonons are included. The inclusion of optical phonons increases the specific heat capacity even more dramatically. As a result, although the thermal conductivity is found to increase, the thermal diffusivity actually decreases and causes the thermal front to propagate slower than if optical phonons are neglected. With the Broido time-scale, the thermal conductivity was found to be larger than the value extracted from experimental data whether or not optical phonon were included. With the Holland time-scale, however, inclusion of optical phonons overpredicted the thermal conductivity, while exclusion underpredicted the same quantity.

# **Declaration of Competing Interest**

The authors declare that they have no known competing financial interests or personal relationships that could have appeared to influence the work reported in this paper.

# **Data Availability**

Data will be made available on request.

# Acknowledgments

This research was funded, in part, by Award No. 2003747 by the National Science Foundation. The Ohio Supercomputer Center (OSC) and the Department of Mechanical and Aerospace Engineering at the Ohio State University are gratefully acknowledged for providing computational resources.

### References

- D.G. Cahill, Analysis of heat flow in layered structures for time domain thermo-reflectance, Rev. Sci. Instrum. 75 (2004) 5119.
- [2] K.T. Regner, D.P. Sellan, Z. Su, C.H. Amon, A.J.H. McGaughey, J.A. Malen, Broadband phonon mean free path contributions to thermal conductivity to thermal conductivity measured using frequency domain themroreflectance, Nat. Commun. 4 (2013) 1640.
- [3] A.J. Minnich, J.A. Johnson, A.J. Schmidt, K. Esfarjani, M.S. Dresselhaus, K.A. Nelson, G. Chen, Thermal conductivity spectroscopy technique to measure phonon mean free paths, Phys. Rev. Lett. 107 (2011) 095901.
- [4] A. Feldman, Algorithm for solutions of the thermal diffusion equation in a stratified medium with a modulated heating source, High Temp. High Press. 31 (1999) 293–298.
- [5] S. Saurav, S. Mazumder, On the determination of thermal conductivity from frequency domain thermoreflectance experiments, J. Heat Transf. 144 (2022) 013501.
- [6] Y.K. Koh, D.G. Cahill, Frequency dependence of the thermal conductivity of semiconductor alloys, Phys. Rev. B 76 (2007) 075207.
- [7] A.J. Minnich, Determining phonon mean free paths from observations of quasiballistic thermal transport, Phys. Rev. Lett. 109 (2012) 205901.
- [8] C. Hua, A.J. Minnich, Transport regimes in quasiballistic heat conduction, Phys. Rev. B 89 (2014) 094302.
- [9] C.L. Tien, A. Majumdar, F.M. Gerner, Microscale Energy Transport, Taylor and Francis, 1998.
- [10] P. Allu, S. Mazumder, Comparative assessment of deterministic approaches to modeling quasiballistic phonon heat conduction in multi-dimensional geometry, Int. J. Therm. Sci. 127 (2018) 181–193.
- [11] Y. Ma, A two-parameter nondiffusive heat conduction model for data analysis in pump-probe experiments, J. Appl. Phys. 116 (2014) 243505.
- [12] A.T. Ramu, J.E. Bowers, A compact heat transfer model based on an enhanced Fourier law for analysis of frequency domain thermoreflectance experiments, Appl. Phys. Lett. 106 (2015) 263102.

- [13] G. Chen, Ballistic-diffusive heat-conduction equations, Phys. Rev. Lett. 86 (11) (2001) 2297–2300.
- [14] A. Mittal, S. Mazumder, Generalized ballistic-diffusive formulation and hybrid  $S_N$ - $P_N$  solution of the boltzmann transport equation for phonons for non-equilibrium heat conduction, J. Heat Transf. 133 (9) (2011) 092402 Article No.
- [15] A. Mittal, S. Mazumder, Hybrid discrete ordinates—spherical harmonics solution to the boltzmann transport equation for phonons for non-equilibrium heat conduction, J. Comput. Phys. 230 (18) (2011) 6977–7001.
- [16] A. Beardo, M.G. Hennessy, L. Sendra, J. Camacho, T.G. Myers, J. Bafaluy, F.X. Alvarez, Phonon hydrodynamics in frequency-domain thermoreflectance experiments, Phys. Rev. B 101 (2020) 075303.
- [17] R.B. Wilson, J.P. Fesser, G.T. Hohensee, D.G. Cahill, Two-channel model for nonequilibrium thermal transport in pump-probe experiments, Phys. Rev. B 88 (2013) 144305.
- [18] R.B. Wilson, D.G. Cahill, Anisotropic failure of fourier theory in time-domain thermoreflectance experiments, Nat. Commun. 5 (2014) 5075.
- [19] S. Mazumder, Boltzmann transport equation based modeling of phonon heat conduction: progress and challenges, in: Annual Review of Heat Transfer, 24, Begell House Publications, 2022, pp. 71–130, doi:10.1615/ AnnualRevHeatTransfer.2022041316.
- [20] R. Li, E. Lee, T. Luo, Physics-informed neural networks for solving multiscale mode-resolved phonon Boltzmann Transport Equation, Mater. Phys. Today 19 (2021) 100429.
- [21] Y. Hu, Y. Shen, H. Bao, Ultra-efficient and parameter-free computation of submicron thermal transport with phonon Boltzmann Transport Equation, Fundam. Res., 2022, doi:10.1016/j.fmre.2022.06.007.
- [22] J-P.M. Peraud, N.G. Hadjiconstantinou, Efficient simulation of multidimensional phonon transport using energy-based variance-reduced monte carlo formulations, Phys. Rev. B 84 (2011) 205331.
- [23] D. Ding, X. Chen, A.J. Minnich, Radial quasiballistic transport in time-domain thermo-reflectance studied using monte carlo simulations, Appl. Phys. Lett. 104 (2014) 143104.
- [24] K.T. Regner, A.J.H. McGaughey, J.A. Malen, Analytical interpretation of nondiffusive phonon transport in thermoreflectance thermal conductivity measurements, Phys. Rev. B 90 (2014) 064302.
- [25] S.A. Ali, S. Mazumder, Phonon Boltzmann Transport Equation based modeling of time domain thermo-reflectance experiments, Int. J. Heat Mass Transf. 107 (2017) 607–621.
- [26] S. Saurav, S. Mazumder, Phonon Boltzmann Transport Equation based modeling of frequency domain thermoreflectance experiments, in: Proceedings of the IMECE2022, Columbus, Ohio, 2022 October 30-November 3, 2022Paper Number IMECE2022-95630.
- [27] M.F. Modest, S. Mazumder, Radiative Heat Transfer, 4th Ed., Academic Press, New York, 2021.
- [28] A. Majumdar, Microscale heat transfer in dielectric thin films, J. Heat Transf. 115 (1993) 7–16.
- [29] S. Mazumder, A. Majumdar, Monte Carlo study of phonon transport in solid thin films including dispersion and polarization, J. Heat Transf. 123 (2001) 740, 750
- [30] S. Mazumder, Numerical Methods for Partial Differential Equations: Finite Difference and Finite Volume Methods, 1st ed., Academic Press, New York, 2016.
- [31] E. Pop, Self-heating and scaling of thin body transistors, Department of Electrical Engineering PhD. Dissertation, Stanford University, 2004.
- [32] A. Mittal, S. Mazumder, Monte Carlo study of phonon heat conduction in silicon thin films including contributions of optical phonons, J. Heat Transf. 132 (2010) 052402.
- [33] S.A. Ali, G. Kollu, S. Mazumder, P. Sadayappan, A. Mittal, Large-scale parallel computation of the phonon boltzmann transport equation, Int. J. Therm. Sci. 86 (2014) 341–351.
- [34] Y. Hu, Y. Shen, H. Bao, Optimized phonon band discretization scheme for efficiently solving the nongray boltzmann transport equation, J. Heat Transf. 144 (7) (2022) 072501.
- [35] K. Esfarjani, J. Garg, G. Chen, Modeling heat conduction from first principles, Ann. Rev. Heat Transf. 17 (2014) 9–47.
- [36] K. Esfarjani, G. Chen, Heat transport in silicon from first-principles calculations, Phys. Rev. B 84 (2011) 085204.
- [37] D.A. Broido, M. Malorny, G. Birner, N. Mingo, Intrinsic lattice thermal conductivity of semiconductors from first principles, Appl. Phys. Lett. 91 (2007) 231922.
- [38] J.Y. Murthy, S.V.J. Narumanchi, J.A. Pascual-Gutierrez, T. Wang, C. Ni, S.R. Mathur, Review of multiscale simulation in submicron heat transfer, Int. J. Multiscale Comput. Eng. 3 (2005) 5–32.
- [39] S. Sinha, K.E. Goodson, Review: multiscale Thermal Modeling in Nanoelectronics, Int. J. Multiscale Comput. Eng. 3 (2005) 107–133.
- [40] A. Ward, D.A. Broido, Intrinsic phonon relaxation times from first principles studies of the thermal conductivities of Si and Ge, Phys. Rev. B 81 (8) (2010) 085205.
- [41] M.G. Holland, Analysis of lattice thermal conductivity, Phys. Rev. 132 (6) (1963) 2461–2471.
- [42] A.S. Henry, G. Chen, Spectral phonon transport properties of silicon based on molecular dynamics simulations and lattice dynamics, J. Comput. Theor. Nanosci, 5 (2) (2008) 141–152.